

An Endoscopic Continuum Testbed for Finalizing System Characteristics of a Surgical Robot for NOTES Procedures

Jiangran Zhao, *Student Member, IEEE*, Xidian Zheng,
Minhua Zheng, Albert J. Shih and Kai Xu*, *Member, IEEE*

Abstract— Natural Orifice Transluminal Endoscopic Surgery (NOTES) has recently attracted lots of attention, promising surgical procedures with fewer complications, better cosmesis, lower pains and faster recovery. Several robotic systems were developed aiming to enable abdominal surgeries in a NOTES manner. Although these robotic systems demonstrated the surgical concept, characteristics which could fully enable NOTES procedures remain unclear. This paper presents the development of an endoscopic continuum testbed for finalizing system characteristics of a surgical robot for NOTES procedures, which include i) deployability (the testbed can be deployed in a folded endoscope configuration and then be unfolded into a working configuration), ii) adequate workspace, iii) sufficient distal dexterity (e.g. suturing capability), and iv) desired mechanics properties (e.g. enough load carrying capability). Continuum mechanisms were implemented in the design and a diameter of 12mm of this testbed in its endoscope configuration was achieved. Results of this paper could be used to form design references for future development of NOTES robots.

I. INTRODUCTION

Although laparoscopic minimally invasive surgery has successfully reduced complication rates, postoperative pain and hospitalization time, surgeons continue to innovate for less surgical invasiveness. NOTES (Natural Orifice Transluminal Endoscopic Surgery) is such a recent advance. In NOTES, an endoscope was often inserted through the patient's natural orifices (e.g. vagina, esophagus and stomach, etc.) to deliver surgical tools to surgical sites for interventions [1]. The elimination of skin incisions in NOTES could lead to better surgical outcomes, such as fewer complications, lower pains, better cosmesis and faster recovery. Recent clinical studies [2] and many animal studies [3] have shown NOTES effective in further diminishing postoperative complications, such as infection, peritoneal adhesion, hernia, etc. However, due to the lack of proper instrumentation, NOTES is only limited to a few surgical paradigms. Due to the promising perspective of NOTES, efforts were made to develop special manual tools [4, 5]. However, since two or more surgical tools shall be

manipulated through a long endoscope in NOTES, robotic assistance seems advantageous and several robotic systems were developed, aiming to enable NOTES for general abdominal surgeries [6-11]. These robotic systems were constructed primarily to demonstrate the feasibility of robot-assisted NOTES. Each prototype followed different design approaches, structural topologies, actuation schemes, etc. Benchmark characteristics which could fully enable NOTES procedures remain unclear.

Towards the goal of realizing NOTES procedures for a wider spectrum of surgical paradigms, this paper presents the development of an endoscopic continuum testbed for finalizing design characteristics of a surgical robot for NOTES procedures, as shown in Fig. 1.

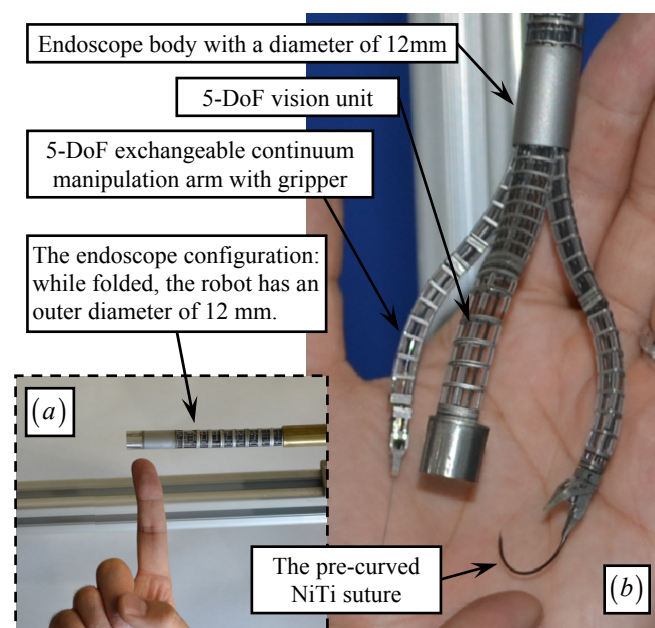


Figure 1. Design of the endoscopic continuum testbed: (a) the folded endoscope configuration and (b) the unfolded working configuration

This testbed is currently pure mechanical with manual actuations. For its endoscope configuration, the current testbed in Fig. 1 has an outer diameter of 12mm, which is comparable to gastroscopes from Olympus® (e.g. GIF-XTQ160 with an outer diameter of 12.9mm). After being deployed into the stomach, the testbed can open its 5-DoF (Degrees of Freedom) vision unit and two 5-DoF exchangeable manipulation arms to form its working configuration. Each manipulation arm is equipped with a gripper and an embedded pre-curved suture made from super elastic NiTi (nickel-titanium) alloy.

This work was supported in part by the National Science Foundation of China Grant #51005146, in part by Shanghai Pujiang Scholar Program #11PJ1405600, and in part by the University of Michigan - Shanghai Jiao Tong University Collaborative Research Fund.

Jiangran Zhao, Xidian Zheng and Kai Xu are with the RII Lab (Lab of Robotics Innovation and Intervention), UM-SJTU Joint Institute, Shanghai Jiao Tong University, Shanghai, 200240, China (asterisk indicates the corresponding author, phone: 8621-34207220; fax: 8621-34206525; emails: zjr318@sjtu.edu.cn, xdzheng@sjtu.edu.cn and k.xu@sjtu.edu.cn).

Minhua Zheng is with the Department of Surgery, Shanghai Jiao Tong University, Shanghai, 200240, China (email: mhzheng@sjtu.edu.cn).

Albert J. Shih is with the Department of Mechanical Engineering, University of Michigan, Ann Arbor, MI, 48109 (email: shiha@umich.edu).

Desired design characteristics of this testbed include i) deployability, ii) adequate workspace, iii) sufficient distal dexterity (e.g. suturing capability), and iv) desired mechanics properties (e.g. enough weight lifting capability). The deployability and system overview were presented in [12]. This paper focuses on workspace analysis and verification of this testbed's suturing capability. Statics analysis will be carried out in the future, whereas preliminary experiments of weights lifting are only briefly presented. This testbed design has an early version as in [13], which was later abandoned due to limited functionality.

This testbed design is inspired by the IREP robot for SPA (Single Port Access) surgeries as in [14-16]. New features introduced in this design include i) performing suturing without using a distal rotary wrist, ii) reducing the overall outer diameter to 12mm, iii) improving backbone arrangements in the manipulation arms, iv) incorporating a continuum vision unit, and v) introducing a consistent actuation scheme for the arms and the vision unit. The use of pre-curved NiTi suture is inspired by the work done by Webster *et al.* [17] and Dupont *et al.* [18] where concentric continuum robots were studied for navigation and therapy delivery.

The paper is organized as follows. Section II summarizes system overview and component descriptions. Nomenclature and kinematics of the continuum manipulation arms are presented in Section III. Section IV focuses on experimental characterization of the in-vitro tissue penetration motions and the simulated knot tying motions, while briefly summarizing the weight lifting experiments. Conclusion is followed in Section V.

II. SYSTEM OVERVIEW AND COMPONENT DESCRIPTIONS

System descriptions of this testbed detailed in [12] are summarized here to make this article standalone. Additional details about the cross section and the suture are also included to make the presentation more understandable.

A. Design Concepts and System Overview

With the existing NOTES robots [6-11] in mind, the authors attempted to develop one with an outer diameter comparable to the commercial gastroscopes (e.g. 12mm). However, functionality of the NOTES robot should be preserved no matter how much the diameter had been reduced. This mechanical testbed was constructed to verify all the desired system characteristics, including deployability, adequate workspace, sufficient distal dexterity and proper stiffness / strength. Properties of this testbed could be evaluated using manual actuations, avoiding the distraction from implementing a complex control system with dozens of servomotors.

Design challenge of this testbed is centered at the outer diameter of its endoscope configuration (currently 12mm). A smaller diameter could lead to less invasiveness and less discomfort during the insertion. However, a smaller diameter brings more design challenges. It will be more difficult to integrate enough DoFs to ensure adequate workspace and dexterity. With more DoFs incorporated within a certain diameter, structures might have to be slimmer and fail to

manipulate sufficient payload with adequate stiffness. Since space within the 12mm diameter is so limited, the authors came up with the cross section design of the endoscope body in order to efficiently utilize the available space as in Fig. 2. Tolerances between the cross sections of the manipulation arms and that of the endoscope are quite loose to ease the insertion of the arms.

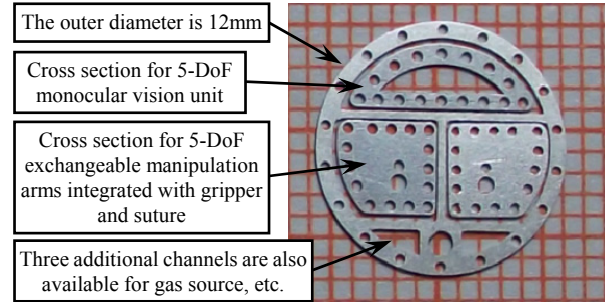


Figure 2. Cross section of the endoscope body of the testbed (background is a piece of graph paper with grids of 1mm x 1mm)

Deployment of this testbed was shown in Fig. 3 and in [12]: (a) the endoscopic testbed could be inserted into a stomach in its folded endoscope configuration; (b) then the vision unit would start extending and bending itself to (c) form a desired pose; (d) the two continuum manipulation arms could then be inserted individually or together to (e, f) form various poses for surgical interventions.

The exchangeable manipulation arms could also be replaced by sensor modules (e.g. an ultrasound probe) or energy sources (e.g. a cautery). And the testbed could be placed at the distal end of an existing endoscope (e.g. the ones as in [19, 20]) for positioning and orienting in the stomach and/or the abdomen.

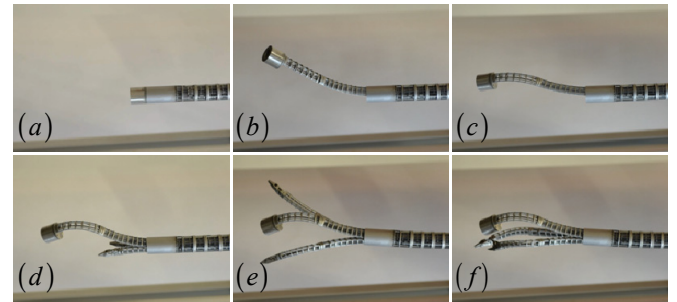


Figure 3. Deployment of the endoscopic continuum testbed

B. Vision Unit, Continuum Arms and Their Actuators

The 5-DoF vision unit and the two 5-DoF exchangeable continuum manipulation arms are shown in Fig. 4. Both the vision unit and the manipulation arms possess continuum segments. Referring to Fig. 7, a structural similarity shared by these continuum segments is that each continuum segment consists of a base disk, an end disk, several spacer disks and several backbones¹. The backbones are thin rods made from super elastic NiTi (nickel-titanium) alloy. They are attached to the end disks and can slide in holes of spacer disks and base

¹ These thin rods can be both pulled and pushed. They hence are all referred to as backbones. Calling them a backbone and tendons might be misleading, leaving the impression that tendons can't be pushed. It's slightly different from the definition of a backbone in [21].

disks. Synchronized pushing and pulling of these backbones deform the segments into desired shapes. Both *segment I* and *segment II* can bend sideward any direction, which is a 2-DoF bending motion. *Segment I* has one additional DoF which is its variable length when extended from the endoscope. This DoF is realized by the feeding/insertion motion of the vision unit and the arms. Namely *segment I* has three DoFs whereas *segment II* has two DoFs. An actuation unit will remain proximal and drive the vision unit and the arms remotely.

The CCD chip intended for the camera head has an outer diameter of 8.0mm and a length of 10.5mm². The CCD chip also has four built-in LEDs for illumination. Camera field of view is determined by lens specifications. The field of view was assembled into the CAD model to make sure grippers of the manipulation arms will be seen.

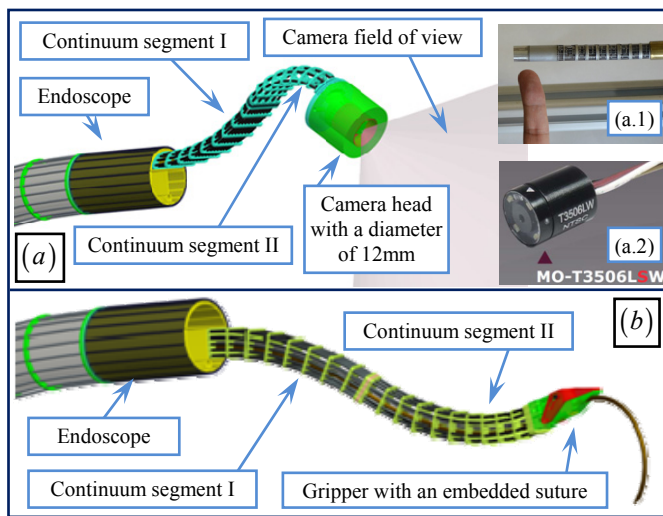


Figure 4. (a) The 5-DoF vision unit: (a.1) the camera head can be fully retracted in the folded endoscope configuration; (a.2) CCD chip with four built-in LEDs; (b) the 5-DoF exchangeable continuum arm

As shown in Fig. 5, one continuum arm with two segments can be pulled out from the testbed. To bend these segments, at least three NiTi backbones are needed for a push-pull actuation. Referring to Fig. 4, many redundant backbones were used in order to improve the stiffness of the continuum arms. The inset (b) in Fig. 5 shows how these redundant backbones can be actuated: backbones of these segments are routed through rigid guiding cannulae and connected to actuation plates; these actuation plates are properly scaled from the segments' disks; manual bending the actuation plates deforms the corresponding segments in the opposite direction. The vision unit is also actuated in a similar way.

C. Super Elastic NiTi Suture

Suturing (including repeated tissue penetration and knot tying) in confined spaces using a traditional rigid circular suture is difficult even when the task was assisted by robots [22-24]. Tissue penetration involves a distal rotation along an axis normal to the suture plane through the suture's center, as shown in Fig. 6(a).

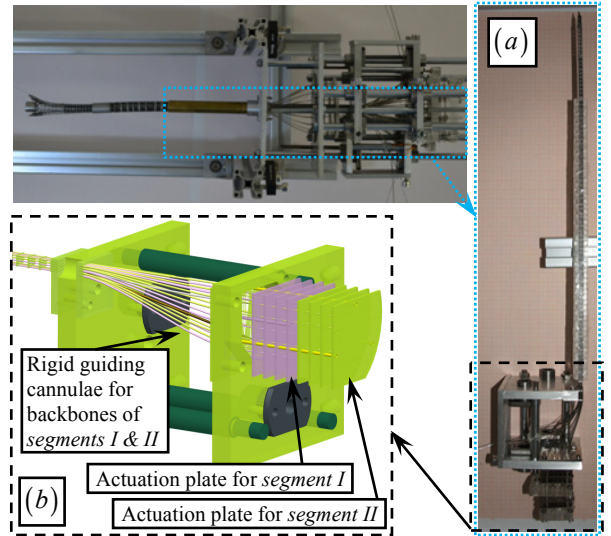


Figure 5. The testbed with its actuation: (a) one continuum arm can be pulled out; (b) actuation scheme of the arms

This testbed uses a pre-curved super elastic NiTi suture to facilitate tissue penetration. While housed in a rigid housing as shown in Fig. 6(b), the suture is forced straight; while pushed outwards, it bends back to its original shape, penetrating tissues in a circular path. A NiTi tube³ with an outer diameter of 0.69mm and an inner diameter of 0.51mm was used as the suture, shown in Fig. 6(c). A suture thread passes the suture with one end hung outside. During tissue penetration, the thread will be brought through the tissue by the non-cutting edge of the suture tip. After penetration, the thread will be picked up by the other arm before the suture is retracted. After the suture is retracted, the thread is left through tissue and ready for knot tying. The related experiments are detailed in Section IV.

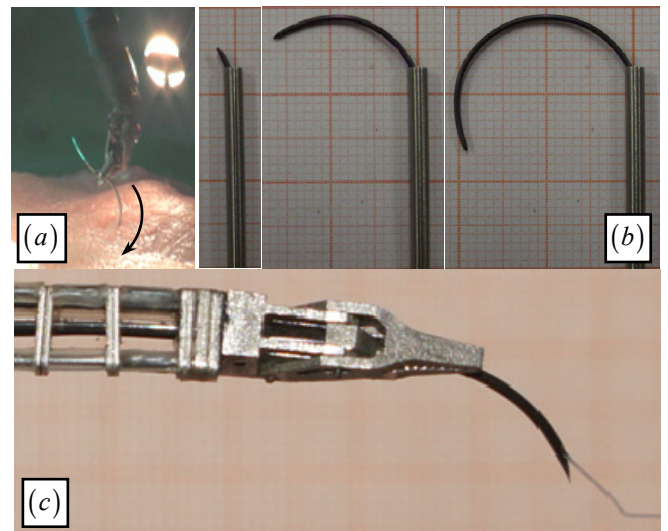


Figure 6. (a) When a rigid circular suture is used, tissue penetration involves a distal rotation as in [24]; (b) whereas when a Ø0.69mm NiTi suture is used, it bends back to its preset circular shape after released from a rigid housing. (c) The thread passes through the channel in the suture so that it can be brought through the tissue for knot tying.

² MO-T3506LSW from the MUSUMI Electronics Corp

³ Superelastic Nitinol Tube – Alloy BB, Memry Corp.

III. NOMENCLATURE AND KINEMATICS

Continuum manipulation arms in Fig. 4 consist of segments as shown in Fig. 7. Thorough analysis of one continuum segment's kinematics can be found in [21, 23, 25-27], based on an underlying assumption of constant bending curvature. This paper extends modeling of such a continuum segment to a case with asymmetric cross section. Kinematics of one segment will be used to assemble the kinematics of the manipulation arm.

Robot workspace is verified with an analysis of the arm's kinematics, whereas the instantaneous kinematics (Jacobian) will be used in Section IV in a simulation to verify the arms' knot-tying capability.

A. Nomenclature and Coordinate Systems

Since these segments are similar, Fig. 9 only shows the t th segment ($t=1$ or 2). Nomenclatures are defined in Table I with coordinate systems of the t th segment defined as below:

- **Base Disk Coordinate System (BDS)** is designated as $\{tb\} \equiv \{\hat{x}_{tb}, \hat{y}_{tb}, \hat{z}_{tb}\}$. It is attached to the base disk of the t th segment, whose XY plane coincides with the base disk and its origin is at the center of the base disk. \hat{x}_{tb} points from the center of the base disk to the first secondary backbone while \hat{z}_{tb} is perpendicular to the base disk. Secondary backbones are numbered according to the definition of δ_{ii} .
- **Bending Plane Coordinate System 1 (BPS1)** is designated as $\{t1\} \equiv \{\hat{x}_{t1}, \hat{y}_{t1}, \hat{z}_{t1}\}$ which shares its origin with $\{tb\}$ and has the continuum segment bending in its XZ plane.
- **Bending Plane Coordinate System 2 (BPS2)** is designated as $\{t2\} \equiv \{\hat{x}_{t2}, \hat{y}_{t2}, \hat{z}_{t2}\}$ obtained from $\{t1\}$ by a rotation about \hat{y}_{t1} such that \hat{z}_{t1} becomes backbone tangent at the end disk. Origin of $\{t2\}$ is at center of the end disk.
- **End Disk Coordinate System (EDS)** $\{te\} \equiv \{\hat{x}_{te}, \hat{y}_{te}, \hat{z}_{te}\}$ is fixed to the end disk of the t th segment. \hat{x}_{te} points from center of the end disk to the first secondary backbone and \hat{z}_{te} is normal to the end disk. $\{te\}$ is obtained from $\{t2\}$ by a rotation about \hat{z}_{t2} .

When the t th and $(t+1)$ th segment are stacked, $\{te\}$ coincides with $\{(t+1)b\}$.

TABLE I. NOMENCLATURE USED IN THIS PAPER

m	Number of secondary backbones
i	Index of the secondary backbones, $i = 1, 2, \dots, m$
t	Index of the segments $t = 1$ or 2 ; numbering of the segments always precedes the secondary backbones.
r_i	Distance from the primary backbone to the i th secondary backbone. r_i can be different for different backbones.
β_i	β_i characterizes the division angle from the i th secondary backbone to the 1st secondary backbone. $\beta_i \equiv 0$ and β_i remain constant once the segment is built.

L_t, L_{ti}	Length of the primary and the i th secondary backbone for the t th segment
\mathbf{q}_t	$\mathbf{q}_t = [q_1 \ q_2 \ \dots \ q_m]^T$ is the actuation length vector in the joint space for the t th segment, where $q_{ii} = L_{ti} - L_t$.
$\theta_t(s)$	The angle of the tangent to the primary backbone in the bending plane for the t th segment. $\theta_t(L_t)$ and $\theta_t(0)$ are designated by θ_{tL} and θ_0 . $\theta_0 = \pi/2$ is a constant.
δ_{ii}	For the t th segment, a right-handed rotation angle from \hat{x}_{ti} about \hat{z}_{ti} to a ray passing through the primary backbone and the i th secondary backbone.
δ_i	$\delta_i \equiv \delta_{i1}$ and $\delta_{ii} = \delta_i + \beta_i$, $i = 1, 2, \dots, m$
${}^l\mathbf{R}_2$	Coordinate transformation matrix frame 2 to frame 1.
${}^{tb}\mathbf{p}_t(s)$	Position vector of a point along the primary backbone in $\{tb\}$. ${}^{tb}\mathbf{p}_t(L_t)$ is the tip position designated by ${}^{tb}\mathbf{p}_{tL}$.

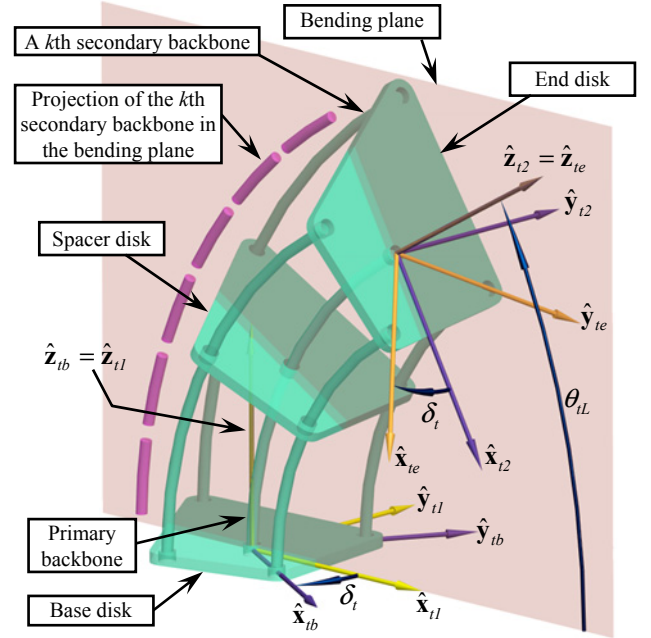


Figure 7. Nomenclature and coordinates of the t th continuum segment

B. Kinematics of the 2-DoF Continuum Segment II

As shown in Fig. 4, *segment II* has two DoFs associated with bending, which can be characterized by a configuration vector $\boldsymbol{\psi}_2 \equiv [\theta_{2L} \ \delta_2]^T$. The assumption of constant bending curvature gives the following:

$${}^{tb}\mathbf{p}_{tL} = \frac{L_t}{\theta_{tL} - \theta_0} \begin{bmatrix} \cos \delta_i (\sin \theta_{tL} - 1) \\ \sin \delta_i (1 - \sin \theta_{tL}) \\ -\cos \theta_{tL} \end{bmatrix}, \quad t = 2 \quad (1)$$

Where ${}^{tb}\mathbf{p}_{tL} = [0 \ 0 \ L_t]^T$ when $\theta_{tL} = \theta_0 = \pi/2$

Rotation matrix ${}^{tb}\mathbf{R}_{te}$ associates $\{te\}$ and $\{tb\}$:

$${}^{tb}\mathbf{R}_{te} = \mathbf{R}(\hat{z}_{tb}, -\delta_i) \mathbf{R}(\hat{y}_{t1}, \theta_0 - \theta_{tL}) \mathbf{R}(\hat{z}_{t2}, \delta_i), \quad t = 2 \quad (2)$$

Where $\mathbf{R}(\hat{\mathbf{n}}, \gamma)$ designates rotation about $\hat{\mathbf{n}}$ by an angle γ .

The instantaneous kinematics is then given as follows, based on the expressions of ${}^{tb}\mathbf{p}_{iL}$ and ${}^{tb}\mathbf{R}_{ie}$:

$$\dot{\mathbf{x}} = \mathbf{J}_{2x\psi} \dot{\boldsymbol{\psi}}_2, \text{ where } \mathbf{J}_{2x\psi} = \begin{bmatrix} \mathbf{J}_{2v}^T & \mathbf{J}_{2\omega}^T \end{bmatrix}^T \quad (3)$$

$$\mathbf{J}_{2v} = \begin{bmatrix} L_2 \cos \delta_2 \frac{(\theta_{2L} - \theta_0) \cos \theta_{2L} - \sin \theta_{2L} + 1}{(\theta_{2L} - \theta_0)^2} & -L_2 \frac{\sin \delta_2 (\sin \theta_{2L} - 1)}{\theta_{2L} - \theta_0} \\ -L_2 \sin \delta_2 \frac{(\theta_{2L} - \theta_0) \cos \theta_{2L} - \sin \theta_{2L} + 1}{(\theta_{2L} - \theta_0)^2} & -L_2 \frac{\cos \delta_2 (\sin \theta_{2L} - 1)}{\theta_{2L} - \theta_0} \\ L_2 \frac{(\theta_{2L} - \theta_0) \sin \theta_{2L} + \cos \theta_{2L}}{(\theta_{2L} - \theta_0)^2} & 0 \end{bmatrix} \quad (4)$$

$$\mathbf{J}_{2\omega} = \begin{bmatrix} -\sin \delta_2 & \cos \delta_2 \cos \theta_{2L} \\ -\cos \delta_2 & -\sin \delta_2 \cos \theta_{2L} \\ 0 & -1 + \sin \theta_{2L} \end{bmatrix}$$

Singularity of $\mathbf{J}_{2x\psi}$ for $\theta_{2L} = \theta_0 = \pi/2$ can be resolved:

$$\lim_{\theta_{2L} \rightarrow \theta_0 = \frac{\pi}{2}} \mathbf{J}_{2x\psi} = \begin{bmatrix} -L_2 \cos \delta_2 / 2 & 0 \\ L_2 \sin \delta_2 / 2 & 0 \\ 0 & 0 \\ -\sin \delta_2 & 0 \\ -\cos \delta_2 & 0 \\ 0 & 0 \end{bmatrix} \quad (5)$$

C. Kinematics of the 3-DoF Continuum Segment I

As shown in Fig. 4, *segment I* has three DoFs. Besides two bending DoFs, feeding of the continuum arm gives the segment a third DoF: the variable length L_1 .

A configuration vector for *segment I* can now be defined as $\boldsymbol{\psi}_1 \equiv [\theta_{1L} \ \delta_1 \ L_1]^T$. Expressions of ${}^{tb}\mathbf{p}_{iL}$ and ${}^{tb}\mathbf{R}_{ie}$ can be still obtained using (1) and (2) for $t = 1$, respectively. The instantaneous kinematics is now given as follows, based on the expressions of ${}^{tb}\mathbf{p}_{iL}$ and ${}^{tb}\mathbf{R}_{ie}$:

$$\dot{\mathbf{x}} = \mathbf{J}_{1x\psi} \dot{\boldsymbol{\psi}}_1, \text{ where } \mathbf{J}_{1x\psi} = \begin{bmatrix} \mathbf{J}_{1v}^T & \mathbf{J}_{1\omega}^T \end{bmatrix}^T \quad (6)$$

$$\mathbf{J}_{1v} = [\mathbf{j}_{1v1} \ \mathbf{j}_{1v2} \ \mathbf{j}_{1v3}]$$

$$\mathbf{J}_{1\omega} = \begin{bmatrix} -\sin \delta_1 & \cos \delta_1 \cos \theta_{1L} & 0 \\ -\cos \delta_1 & -\sin \delta_1 \cos \theta_{1L} & 0 \\ 0 & -1 + \sin \theta_{1L} & 0 \end{bmatrix} \quad (7)$$

Where \mathbf{j}_{1v1} , \mathbf{j}_{1v2} and \mathbf{j}_{1v3} are as the following:

$$\mathbf{j}_{1v1} = \begin{bmatrix} L_1 \cos \delta_1 \frac{(\theta_{1L} - \theta_0) \cos \theta_{1L} - \sin \theta_{1L} + 1}{(\theta_{1L} - \theta_0)^2} \\ -L_1 \sin \delta_1 \frac{(\theta_{1L} - \theta_0) \cos \theta_{1L} - \sin \theta_{1L} + 1}{(\theta_{1L} - \theta_0)^2} \\ L_1 \frac{(\theta_{1L} - \theta_0) \sin \theta_{1L} + \cos \theta_{1L}}{(\theta_{1L} - \theta_0)^2} \end{bmatrix} \quad (8)$$

$$\mathbf{j}_{1v2} = \begin{bmatrix} -L_1 \sin \delta_1 (\sin \theta_{1L} - 1) / (\theta_{1L} - \theta_0) \\ -L_1 \cos \delta_1 (\sin \theta_{1L} - 1) / (\theta_{1L} - \theta_0) \\ 0 \end{bmatrix} \quad (9)$$

$$\mathbf{j}_{1v3} = \begin{bmatrix} \cos \delta_1 (\sin \theta_{1L} - 1) / (\theta_{1L} - \theta_0) \\ \sin \delta_1 (1 - \sin \theta_{1L}) / (\theta_{1L} - \theta_0) \\ -\cos \theta_{1L} / (\theta_{1L} - \theta_0) \end{bmatrix} \quad (10)$$

Singularity of $\mathbf{J}_{1x\psi}$ for $\theta_{1L} = \theta_0 = \pi/2$ can be resolved:

$$\lim_{\theta_{1L} \rightarrow \theta_0 = \frac{\pi}{2}} \mathbf{J}_{1x\psi} = \begin{bmatrix} -L_2 \cos \delta_2 / 2 & 0 & 0 \\ L_2 \sin \delta_2 / 2 & 0 & 0 \\ 0 & 0 & 1 \\ -\sin \delta_2 & 0 & 0 \\ -\cos \delta_2 & 0 & 0 \\ 0 & 0 & 0 \end{bmatrix} \quad (11)$$

D. Kinematics of the 5-DoF Continuum Arm

Kinematics of the 5-DoF continuum arm can be obtained by assembling kinematics from previous sections. Coordinate systems assigned for the arm is shown in Fig. 8, based on their definitions as in Section III.A.

The configuration vector of the arm can now be defined as $\boldsymbol{\xi} = [\boldsymbol{\psi}_2^T \ \boldsymbol{\psi}_1^T]^T = [\theta_{2L} \ \delta_2 \ \theta_{1L} \ \delta_1 \ L_1]^T$. Tip position of the gripper in world coordinate $\{w\}$ can be written as follows:

$${}^w\mathbf{p}_g = {}^w\mathbf{p}_{arm} + {}^{1b}\mathbf{p}_{1L} + {}^{1b}\mathbf{R}_{2b} \left({}^{2b}\mathbf{p}_{2L} + {}^{2b}\mathbf{R}_{2e} {}^{2e}\mathbf{p}_g \right) \quad (12)$$

Where ${}^w\mathbf{p}_{arm}$ is the translation from $\{w\}$ to $\{1b\}$, ${}^{2e}\mathbf{p}_g$ is the gripper tip position in $\{2e\}$ and ${}^{2e}\mathbf{p}_g = [0 \ 0 \ 15mm]^T$.

Jacobian matrix can be derived by writing linear velocity and angular velocity of the gripper as follows:

$${}^w\mathbf{v}_g = \mathbf{J}_{1v} \dot{\boldsymbol{\psi}}_1 + \mathbf{J}_{1\omega} \dot{\boldsymbol{\psi}}_1 \times \left({}^{1b}\mathbf{R}_{2b} {}^{2b}\mathbf{p}_{2L} + {}^{1b}\mathbf{R}_{2e} {}^{2e}\mathbf{p}_g \right) + {}^{1b}\mathbf{R}_{2b} \left(\mathbf{J}_{2v} \dot{\boldsymbol{\psi}}_2 + \mathbf{J}_{2\omega} \dot{\boldsymbol{\psi}}_2 \times \left({}^{2b}\mathbf{R}_{2e} {}^{2e}\mathbf{p}_g \right) \right) \quad (13)$$

$${}^w\boldsymbol{\omega}_g = \mathbf{J}_{1\omega} \dot{\boldsymbol{\psi}}_1 + {}^{1b}\mathbf{R}_{2b} \mathbf{J}_{2\omega} \dot{\boldsymbol{\psi}}_2 \quad (14)$$

Where ${}^{1b}\mathbf{R}_{2e} = {}^{1b}\mathbf{R}_{2b} {}^{2b}\mathbf{R}_{2e}$

Then the Jacobian can be written as follows:

$${}^w\dot{\mathbf{x}} = \mathbf{J}_{x\xi} \dot{\boldsymbol{\xi}} \quad (15)$$

$$\mathbf{J}_{x\xi} = \begin{bmatrix} {}^{1b}\mathbf{R}_{2b} \left(\mathbf{J}_{2v} - \left[{}^{2b}\mathbf{R}_{2e} {}^{2e}\mathbf{p}_g \right]^\times \mathbf{J}_{2\omega} \right) \mathbf{J}_{1v} - \mathbf{T}_1 \mathbf{J}_{1\omega} \\ {}^{1b}\mathbf{R}_{2b} \mathbf{J}_{2\omega} \mathbf{J}_{1\omega} \end{bmatrix} \quad (16)$$

Where $\mathbf{T}_1 = \left[{}^{1b}\mathbf{R}_{2b} {}^{2b}\mathbf{p}_{2L} + {}^{1b}\mathbf{R}_{2e} {}^{2e}\mathbf{p}_g \right]^\times$ and $[\mathbf{p}]^\times$ is the skew symmetric matrix of a vector \mathbf{p} .

Using structural parameters of the arm summarized in

Table II, translational workspace of the arm can be generated by scanning its joint space, as shown in Fig. 9. A cube of 50mm×50mm×50mm can be enveloped by the workspace of both arms. This volume is required by a cholecystectomy according to [14, 15].

TABLE II. JOINT VARIABLE LIMITS AND STRUCTURAL CONSTANTS

For both segments:	$\theta_{iL} \in [0, \pi/2]$	$\delta_i \in [-\pi, \pi]$
Configuration vector $\xi = [\theta_{2L} \ \delta_2 \ \theta_{1L} \ \delta_1 \ L_1]^T$		
$L_1 \in [25mm, 70mm]$	$L_2 = 30mm$	${}^{2e}\mathbf{p}_g = [0 \ 0 \ 15mm]^T$

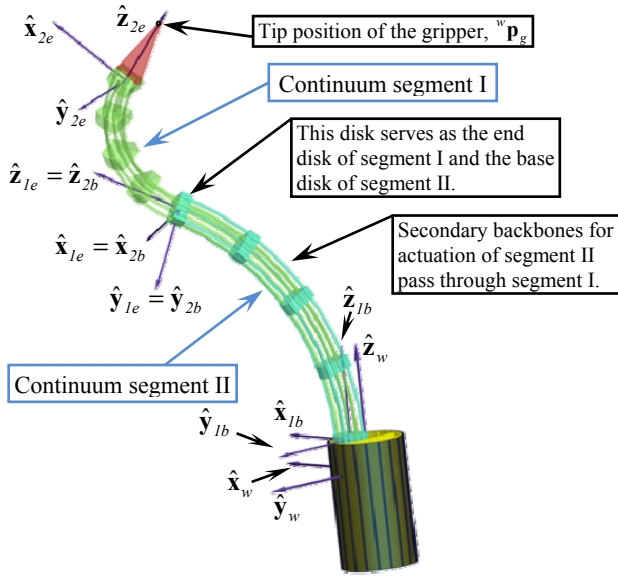


Figure 8. Coordinate systems of the 5-DoF continuum manipulation arm

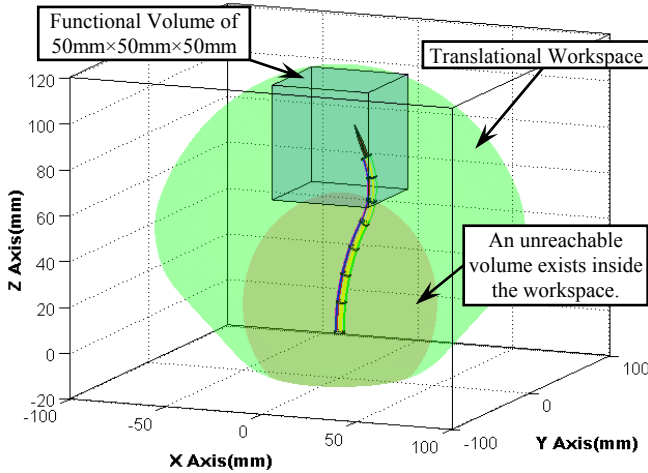


Figure 9. Translational workspace of the manipulation arm

IV. EXPERIMENTAL CHARACTERIZATION

This testbed was constructed to verify and finalize system characteristics of a surgical robot for NOTES procedures. Deployability of this testbed was presented in [12] and shown in Fig. 3. Workspace is shown adequate as in Fig. 9. Suturing capability of this testbed involves tissue penetration and knot tying, which will be demonstrated in Section IV.A and Section

IV.B respectively. Load carrying capability will be briefly qualitatively shown in Section IV.C.

A. Tissue Penetration

In-vitro tissue penetration experiments were firstly carried out on a silicone phantom as shown in Fig. 10. While released from the gripper, the suture penetrated the phantom tissue in a circular path. The inset (a) showed that the non-cutting edge of the suture brought the thread to the other side of the tissue. The inset (b) showed that after retracting the suture, the thread was still kept on the other side of the tissue; the other arm can easily pick it up for knot tying.

The tissue penetration experiments were then repeated on a porcine stomach as shown in Fig. 11: (a) the gripper approached the stomach wall and the NiTi suture was pushed outwards; (b) the stomach was apparently quite tough and the resistance even started twisting the arm; (c) the NiTi suture was eventually powered through the tissue, bringing the thread to the other side of the tissue as well.

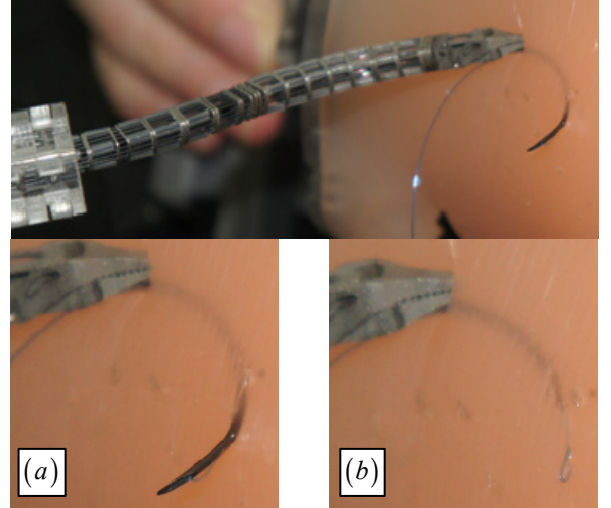


Figure 10. In-vitro tissue penetration experiments on a silicone phantom

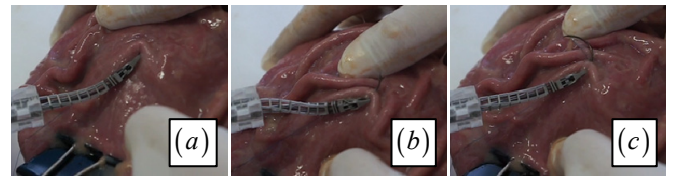


Figure 11. In-vitro tissue penetration experiments on a porcine stomach

B. Simulation Verification of Knot Tying

Suturing capability involves repeated tissue penetration and knot tying. With tissue penetration verified in the previous section, the knot tying capability will be verified here. Since the current testbed was not motorized, knot tying capability was not verified directly on the testbed. Instead, it was verified by an interactive simulation, as shown in Fig. 12.

Two Phantom Omni[®] devices from the Sensable Inc. were used for control inputs. The two Omni devices were firstly registered to the world coordinate of the endoscopic testbed. Pseudo-inverse of the instantaneous kinematics from Section

III.D was then used to drive both arms to follow the inputs from the Omni devices.

The knot tying simulation also includes the modeling of surgical threads, such as those in [28, 29]. The modeling approach in [29] was adopted in this paper, including thread configuration calculation, collision detection, etc. Insets (a) ~ (e) in Fig. 12 showed a complete process of tying a single square knot: (a) two ends of one thread hung out the tissue; (b) the right arm picked up one end (end I) and (c) wrapped it around the left arm; (d) the right arm passed the other end (end II) of the thread to the left arm and picked end I from the other side of the left arm; (e) the knot was formed by tightening the threads.

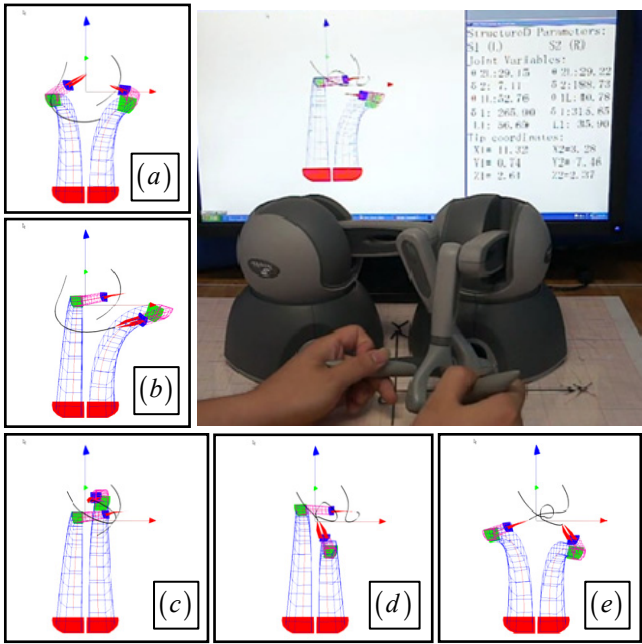


Figure 12. Simulated knot tying using the dual continuum arms under the control inputs from two of Phantom Omni® devices

C. Weight Lifting

Weight-lifting experiments were carried out to determine the strength of such a continuum arm. And it might be possible to find a way to compensate for the payload-caused deflection as in [30]. As shown in Fig. 13, one segment successfully lifted 200 grams, whereas two segments were able to lift 50 grams. Due to the inherent compliance of continuum arms, weight lifting capability deteriorated with an increasing total length of the arm. Quantitative mechanics analysis of the arms will be carried out in the future.

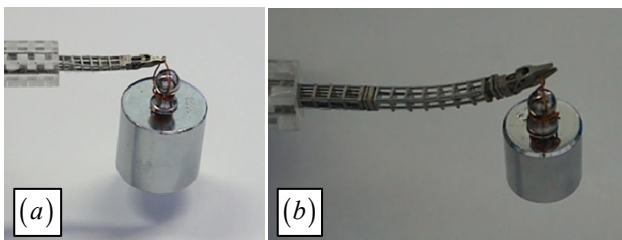


Figure 13. Payload tests of the continuum manipulation arm: (a) 200 grams were lifted using one segment; (b) 50 grams were lifted using two segments;

V. CONCLUSION AND FUTURE WORK

This paper presented the development of an endoscopic continuum testbed for finalizing system characteristics of a surgical robot for NOTES procedures. Critical characteristics include i) deployability, ii) adequate workspace, iii) sufficient distal dexterity (e.g. suturing capability), and iv) desired mechanics properties (e.g. enough load carrying capability).

With deployability of this testbed shown previously as in [12], this article focuses on kinematics analysis to verify design requirements regarding workspace and distal dexterity.

Results obtained in Section III indicate that workspace of the continuum manipulation arms is big enough for typical abdominal procedures such as cholecystectomy. Moreover, results also suggest it is possible for this testbed design to realize suturing without incorporating a distal rotary wrist: tissue penetration was achieved using a pre-curved super elastic NiTi suture and knot tying was verified by the interactive simulation of the dual 5-DoF continuum arms.

Preliminary weight lifting experiments were also carried out on the testbed.

There are yet many to be done to fully understand the advantages and disadvantages of this testbed design. Firstly, understanding on the tissue penetration using the pre-curved NiTi suture should be furthered by modeling the interaction between the suture and surrounding tissues. An optimization could be formulated towards the suture's preset shape for better penetrating behaviors. Secondly the continuum arm should be modeled in details to reveal the mechanics properties of the asymmetric structure, such as stiffness and load carrying capabilities in different directions. Results might suggest a more efficient way to utilize the available space within the endoscope.

It is the hope that a surgical robot for NOTES could be built in the future, incorporating all the improvements based on the results obtained from this testbed. Motorization and teleoperative control of such a surgical robot can then be investigated.

ACKNOWLEDGMENT

The authors would like to thank Dr. Bruce L. J. Tai and Dr. Yancheng Wang from Department of Mechanical Engineering, the University of Michigan Ann Arbor for grinding the tip of the NiTi sutures.

REFERENCES

- [1] A. N. Kallou, V. K. Singh, S. B. Jagannath, H. Niyama, S. L. Hill, C. A. Vaughn, C. A. Magee, and S. V. Kantsevoy, "Flexible Transgastric Peritoneoscopy: a Novel Approach to Diagnostic and Therapeutic Interventions in the Peritoneal Cavity," *Gastrointestinal Endoscopy*, vol. 60, No.1, pp. 114-117, July 2004.
- [2] S. Horgan, J. P. Cullen, M. A. Talamini, Y. Mintz, A. Ferreres, G. R. Jacobsen, B. Sandler, J. Bosia, T. Savides, D. W. Easter, M. K. Savu, S. L. Ramamoorthy, E. Whitcomb, S. Agarwal, E. Lukacz, G. Dominguez, and P. Ferraina, "Natural Orifice Surgery: Initial Clinical Experience," *Surgical Endoscopy*, vol. 23, No.7, pp. 1512-1518, July 2009.
- [3] E. D. Flora, T. G. Wilson, I. J. Martin, N. A. O'Rourke, and G. J. Maddern, "A Review of Natural Orifice Transluminal Endoscopic

- Surgery (NOTES) for Intra-abdominal Surgery: Experimental Models, Techniques, and Applicability to the Clinical Setting," *Annals of Surgery*, vol. 247, No.4, pp. 583-602, April 2008.
- [4] B. Hu, S. Chung, L. C. L. Sun, K. Kawashima, T. Yamamoto, P. B. Cotton, C. J. Gostout, R. H. Hawes, A. N. Kalloo, S. V. Kantsevoy, and P. J. Pasricha, "Eagle Claw II: a Novel Endosuture Device that Uses a Curved Needle for Major Arterial Bleeding: a Bench Study," *Gastrointestinal Endoscopy*, vol. 62, No.2, pp. 266-270, 2005.
- [5] O. R. Meireles, S. V. Kantsevoy, L. R. Assumpcao, P. Magno, X. Dray, S. A. Giday, A. N. Kalloo, E. J. Hanly, and M. R. Marohn, "Reliable Gastric Closure after Natural Orifice Transluminal Endoscopic Surgery (NOTES) Using a Novel Automated Flexible Stapling Device," *Surgical Endoscopy*, 2008.
- [6] S. C. Low, S. W. Tang, Z. M. Thant, L. Phee, K. Y. Ho, and S. C. Chung, "Master-Slave Robotic System for Therapeutic Gastrointestinal Endoscopic Procedures," in *Annual International Conference of the IEEE Engineering in Medicine and Biology Society (EMBS)*, New York, NY, USA, 2006, pp. 3850-3853.
- [7] D. J. Abbott, C. Becke, R. I. Rothstein, and W. J. Peine, "Design of an Endoluminal NOTES Robotic System," in *IEEE/RSJ International Conference on Intelligent Robots and Systems (IROS)*, San Diego, CA, USA, 2007, pp. 410 - 416.
- [8] K. Harada, E. Susilo, A. Menciassi, and P. Dario, "Wireless Reconfigurable Modules for Robotic Endoluminal Surgery," in *IEEE International Conference on Robotics and Automation (ICRA)*, Kobe, Japan, 2009, pp. 2699-2704.
- [9] A. C. Lehman, J. Dumpert, N. A. Wood, L. Redden, A. Q. Visty, S. Farritor, B. Varnell, and D. Oleynikov, "Natural Orifice Cholecystectomy using a Miniature Robot," *Surgical Endoscopy*, vol. 23, No.2, pp. 260-266, Feb 2009.
- [10] G. Tortora, A. Dimitracopoulos, P. Valdastrì, A. Menciassi, and P. Dario, "Design of Miniature Modular in vivo Robots for Dedicated Tasks in Minimally Invasive Surgery," in *IEEE/ASME International Conference on Advanced Intelligent Mechatronics (AIM)*, Budapest, Hungary, 2011, pp. 327-332.
- [11] S. Tognarelli, M. Salerno, G. Tortora, C. Quaglia, P. Dario, and A. Menciassi, "An Endoluminal Robotic Platform for Minimally Invasive Surgery," in *IEEE / RAS-EMBS International Conference on Biomedical Robotics and Biomechatronics (BIOROB)*, Roma, Italy, 2012, pp. 7-12.
- [12] K. Xu, J. Zhao, and A. J. Shih, "Development of an Endoscopic Continuum Robot to Enable Transgastric Surgical Obesity Treatment," in *International Conference on Intelligent Robotics and Applications (ICIRA)* Montreal, Quebec, Canada, 2012, pp. 589-600.
- [13] K. Xu, J. Zhao, J. Geiger, A. J. Shih, and M. Zheng, "Design of an Endoscopic Stitching Device for Surgical Obesity Treatment Using a N.O.T.E.S Approach," in *IEEE/RSJ International Conference on Intelligent Robots and Systems (IROS)*, San Francisco, CA, USA, 2011, pp. 961-966.
- [14] K. Xu, R. E. Goldman, J. Ding, P. K. Allen, D. L. Fowler, and N. Simaan, "System Design of an Insertable Robotic Effector Platform for Single Port Access (SPA) Surgery," in *IEEE/RSJ International Conference on Intelligent Robots and Systems (IROS)*, St. Louis, MO, USA, 2009, pp. 5546-5552.
- [15] J. Ding, R. E. Goldman, K. Xu, P. K. Allen, D. L. Fowler, and N. Simaan, "Design and Coordination Kinematics of an Insertable Robotic Effectors Platform for Single-Port Access Surgery," *IEEE/ASME Transactions on Mechatronics*, vol. Early Access Articles 2012.
- [16] A. Bajo, R. E. Goldman, L. Wang, D. L. Fowler, and N. Simaan, "Integration and Preliminary Evaluation of an Insertable Robotic Effectors Platform for Single Port Access Surgery," in *IEEE International Conference on Robotics and Automation (ICRA)*, Saint Paul, MN, USA, 2012, pp. 3381-3387.
- [17] R. J. Webster, J. M. Romano, and N. J. Cowan, "Mechanics of Precurved-Tube Continuum Robots," *IEEE Transactions on Robotics*, vol. 25, No.1, pp. 67-78, Feb 2009.
- [18] P. E. Dupont, J. Lock, B. Itkowitz, and E. Butler, "Design and Control of Concentric-Tube Robots," *IEEE Transactions on Robotics*, vol. 26, No.2, pp. 209-225, April 2010.
- [19] A. Degani, H. Choset, A. Wolf, and M. A. Zenati, "Highly Articulated Robotic Probe for Minimally Invasive Surgery," in *IEEE International Conference on Robotics and Automation (ICRA)*, Orlando, Florida, 2006, pp. 4167- 4172.
- [20] A. J. Loeve, D. H. Plettenburg, P. Breedveld, and J. Dankelman, "Endoscope Shaft-Rigidity Control Mechanism: "FORGUIDE"," *IEEE Transactions on Biomedical Engineering*, vol. 59, No.2, pp. 542-551, Feb 2012.
- [21] B. A. Jones and I. D. Walker, "Kinematics for Multisection Continuum Robots," *IEEE Transactions on Robotics and Automation*, vol. 22, No.1, pp. 43-55, Feb 2006.
- [22] A. Kapoor, N. Simaan, and R. H. Taylor, "Suturing in Confined Spaces: Constrained Motion Control of a Hybrid 8-DoF Robot," in *International Conference on Advanced Robotics (IACR)*, Seattle, USA, 2005, pp. 452-459.
- [23] N. Simaan, K. Xu, A. Kapoor, W. Wei, P. Kazanzides, P. Flint, and R. H. Taylor, "Design and Integration of a Telerobotic System for Minimally Invasive Surgery of the Throat " *International Journal of Robotics Research*, vol. 28, No.9, pp. 1134-1153, 2009.
- [24] C. Staub, T. Osa, A. Knoll, and R. Bauernschmitt, "Automation of Tissue Piercing using Circular Needles and Vision Guidance for Computer Aided Laparoscopic Surgery," in *IEEE International Conference on Robotics and Automation (ICRA)*, Anchorage, Alaska, USA, 2010, pp. 4585-4590.
- [25] K. Xu and N. Simaan, "An Investigation of the Intrinsic Force Sensing Capabilities of Continuum Robots," *IEEE Transactions on Robotics*, vol. 24, No.3, pp. 576-587, June 2008.
- [26] K. Xu and N. Simaan, "Intrinsic Wrench Estimation and Its Performance Index of Multi-Segment Continuum Robots," *IEEE Transactions on Robotics*, vol. 26, No.3, pp. 555-561, June 2010.
- [27] R. J. Webster and B. A. Jones, "Design and Kinematic Modeling of Constant Curvature Continuum Robots: A Review " *International Journal of Robotics Research*, vol. 29, No.13, pp. 1661-1683, Nov 2010.
- [28] J. Phillips, A. Ladd, and L. E. Kavraki, "Simulated Knot Tying," in *IEEE International Conference on Robotics and Automation (ICRA)*, Washington, DC, USA, 2002, pp. 841-846.
- [29] J. Brown, J.-C. Latombe, and K. Montgomery, "Real-Time Knot-Tying Simulation," *The Visual Computer*, vol. 20, No.2-3, pp. 165-179, 2004.
- [30] K. Xu and N. Simaan, "Analytic Formulation for the Kinematics, Statics and Shape Restoration of Multibackbone Continuum Robots via Elliptic Integrals," *Journal of Mechanisms and Robotics*, vol. 2, Feb 2010.